

# FERMI-LAT OBSERVATION OF THE PULSAR J2021+3651

Giovanni Cozzolongo

20 April 2021

## Abstract

The Fermi-LAT observation of the J2021+3651 pulsar has been reported. The observation of the energy distribution and the mapping of photons in different energy ranges have been made. Then the  $Z_n^2$  test has been used to estimate the pulsar's rotational frequency and its first derivative respect to time. Thus the latter was used to make histograms of the rotation phase. In particular, the differences have been highlighted between the low and high energies cases. Afterwards I have used the dipole emission model to estimate pulsar characteristic quantities such as the minimum magnetic field strength, the characteristic age and the rotational brightness. Finally, J2021+3651 has been put in the  $P-\dot{P}$  diagram, along with some radio pulsars from the Australia Telescope National Facility (ATNF) catalog.

## Contents

### 1 Introduction

### 2 Theoretical notes

### 3 Observation and data preparation

### 4 Energy distribution and photons maps

### 5 Timing analysis

### 6 $P-\dot{P}$ diagram

### 7 Conclusions

## References

## 1 Introduction

A pulsar is a highly magnetized rotating neutron star that emits beams of electromagnetic radiation out of its magnetic poles. This radiation can be observed when a beam of emission is pointing towards the Earth.

The data from the Large Area Telescope (LAT) on the *Fermi Gamma-ray Space Telescope* has been used. The detection is made by the pair conversion, which is the primary interaction of photons with matter in the Fermi energy range. It allow a determination of the incident photon directions via the reconstruction of the trajectories of the resulting electron and positron pairs.

The incident radiation passes through an anticoincidence shield, which is sensitive to charged particles, then through thin layers of high-Z material. The resulting electron and positron energies are then measured by a calorimeter.

## 2 Theoretical notes

The energy released by the pulsars comes from their rotational energy. At large distance the pulsar can be approximated by a rotational magnetic dipole. Let  $c$  be the speed of light,  $I$  the moment of inertia,  $\Omega$  the angular frequency,  $P$  the period of rotation and  $m_\perp$  the magnetic moment component perpendicular to the rotational axis of the pulsar (considered as a uniformly magnetized sphere). Then from the rotational energy

$$E_{rot} = \frac{1}{2} I \Omega^2 = \frac{2\pi^2 I}{P^2}$$

follows that

$$\boxed{\frac{dE_{rot}}{dt} = -\frac{4\pi^2 I \dot{P}}{P^3}}. \quad (1)$$

From the Larmor formula, the radiated power by the magnetic dipole  $P_{rad}$  is

$$P_{rad} = \frac{2}{3} \frac{\ddot{m}_\perp^2}{c^3} = \frac{2}{3} \frac{m_\perp^2 \Omega^4}{c^3} = \frac{2}{3} \frac{m_\perp^2}{c^3} \left(\frac{2\pi}{P}\right)^4 = \frac{2}{3c^3} [BR^3 \sin(\alpha)]^2 \left(\frac{2\pi}{P}\right)^4 \quad (2)$$

where  $B$  is the magnetic field intensity,  $R$  is the radius of the pulsar and  $\alpha$  is the inclination angle between the rotation and the magnetic axes.

Equating eqs.(1) and (2) with the sign changed, follows that

$$\begin{aligned} \frac{dE_{rot}}{dt} = -P_{rad} \Rightarrow B \geq \sqrt{\frac{3c^3 I}{8\pi^2 R^6}} \sqrt{P\dot{P}} \Rightarrow \\ \Rightarrow \boxed{\frac{B}{G} \geq 3.2 \times 10^{19} \sqrt{\frac{P\dot{P}}{s}}} \quad (3) \end{aligned}$$

where  $G$  and  $s$  are respectively the gauss and the second units. In the last step, the constants for the canonical pulsar were inserted:  $R \approx 10^6$  cm and  $I \approx 10^{45}$  g cm<sup>2</sup>.

Moreover

$$P\dot{P} = \frac{8\pi^2 R^6 (B \sin(\alpha))^2}{3c^3 I}.$$

Let  $P_0$  be the initial value of the period and  $\tau$  the characteristic age of the pulsar. From the integral of the identity  $P dP = P\dot{P} dt$  over  $\tau$  follows that

$$\begin{aligned} \int_{P_0}^P P' dP' = \int_0^\tau P\dot{P} dt = P\dot{P} \int_0^\tau dt \Rightarrow \\ \Rightarrow \frac{P^2 - P_0^2}{2} = P\dot{P}\tau. \end{aligned}$$

Now let's assume that  $P_0^2 \ll P^2$ . Thus

$$\boxed{\tau = \frac{P}{2\dot{P}}}. \quad (4)$$

### 3 Observation and data preparation

**Observation** The data that were used for the analysis go from September 21th, 2008 to December 20th, 2008.

**Data selections** Fermitools (more about [1]) have been used to considered only photons within 3 degrees Region Of Interest (ROI), which is

roughly the Point Spread Function at 100 MeV. The zenith angle is 90 degrees, in order to reduce the contribution of Earth Limb gammas photons contamination. For the same reason, the rocking angle value has been considered less than 52 degrees, as suggested here [2].

Only photons with energy above 100 MeV have been considered. Indeed, at those energies, there is a non-negligible positive bias in the LAT energy reconstruction. For further references see [3].

**Events' times corrections** Arrival time of photons to spacecraft was corrected by the Fermitools. First of all, the correction was made according to the position of the spacecraft, which is the so called geometric delay. This correction consists in finding the time that the photon would take to reach the solar system barycenter. There are also relativistic effects to take in consideration: the Shapiro delay in the solar system, aberration due to the motion of the spacecraft around the Earth and the motion of the Earth around the Sun. In addition to the previous corrections, there is also the relativistic delay at the source, but for binary pulsars only. [4]

### 4 Energy distribution and photons maps

From the energy distribution of the photons in Fig. 1, a significant presence of gamma rays can be observed. Photon maps with photons having energy higher than 300 MeV and those higher than 1 GeV are showed in Fig. 2. It can be seen how the high-energy photons tend to come from a point source located at approximately (RA, Dec) = (305, 36) (J2000) in decimal degrees. While low-energy photons, although concentrated in the central source, cover roughly the whole area of view. This points out that there is a gamma-ray source at the center.

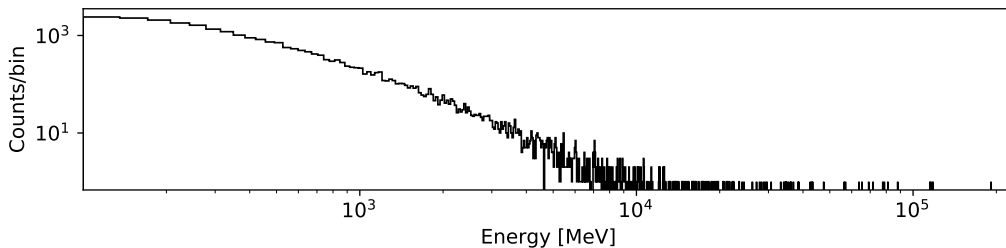


Figure 1: Photon energy histogram above 100 MeV. The thickness of the bin is about 35 MeV.

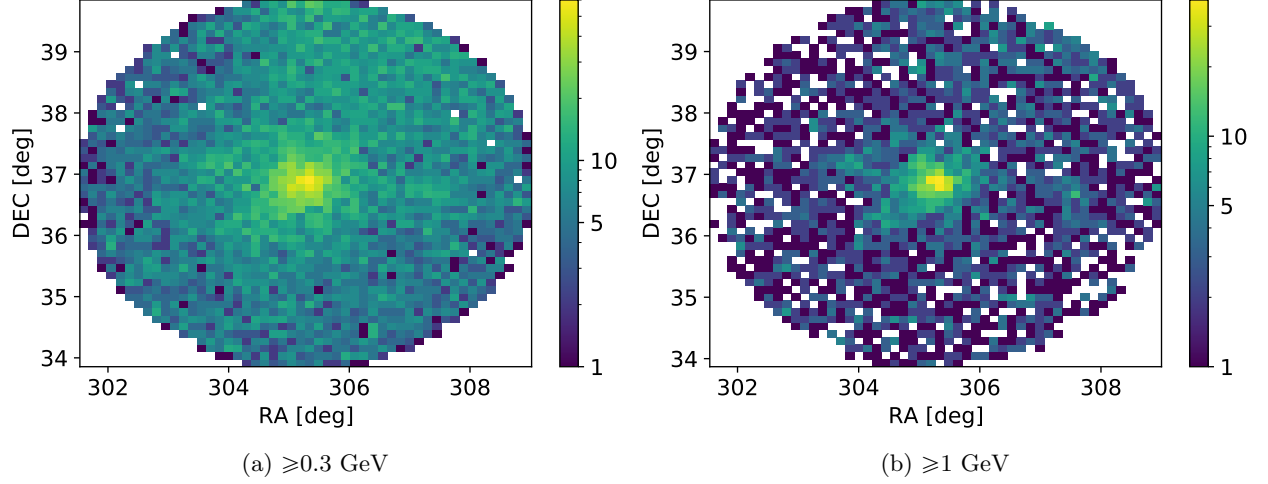


Figure 2: Photons maps expressed in RA and DEC for the energies ranges specified under each one. The thickness of the 50 vertical bins is about 0.14 degree, while the 50 vertical ones are about 0.12 degree.

## 5 Timing analysis

**Rotational parameters** The differentiate of the number of turns made by the pulsar is

$$dN = f(t)dt \approx [f(t_0) + \dot{f}(t_0)(t - t_0)]dt \quad (5)$$

where  $t_0$  is called epoch. To find the fractional part of the number of turns  $N$  (which is the phase) it can be used the timing model

$$\phi_i(t) \approx \phi(t_0) + f\Delta t_i + \frac{1}{2}\dot{f}\Delta t_i^2 \quad (6)$$

where  $i$  goes from 1 to  $N_i$ , the latter is the number of photons and  $\phi(t_0)$  is a constant. The pulsar frequency  $f$  and its first derivative respect to time  $\dot{f}$  are the timing solutions.  $\Delta t_i$  is the difference between the arrival time of the  $i^{th}$  photon and  $t_0$ .  $Z_n^2$  test was used to estimate the rotational parameters, which are the frequency  $f$  and its first derivation respect to time  $\dot{f}$ .

The following statistical variable was used

$$Z_n^2 = \frac{2}{N_i} \sum_{k=1}^n \left[ \left( \sum_{j=1}^{N_i} \cos((2\pi k \phi_j)) \right)^2 + \left( \sum_{j=1}^{N_i} \sin((2\pi k \phi_j)) \right)^2 \right]$$

where  $n$  is the chosen number of harmonics. See for details [5].

$Z_n^2$  was calculated for different values of  $f$  and  $\dot{f}$  separated by intervals. Then the pair with the higher  $Z_n^2$  was chosen.

The results with  $n = 4$  are

$$f = (9639344919 \pm 1) \times 10^{-9} \text{ s}^{-1} \quad (7)$$

$$\dot{f} = (88855 \pm 3) \times 10^{-16} \text{ s}^{-2} \quad (8)$$

where uncertainties are, respectively, the intervals which separates the tested values of  $f$  and  $\dot{f}$ .

Now expanding  $P$  with the Taylor's theorem until the first order

$$P = \frac{1}{f} = \frac{1}{f(t_0)} - \frac{\dot{f}(t_0)}{f^2(t_0)}(t - t_0) + O((t - t_0)^2)$$

where  $t_0 \approx 247536491 \text{ s}$  (the central time of the time interval), it follows that

$$P = \frac{1}{f(t_0)}, \quad \dot{P} = -\frac{\dot{f}(t_0)}{f^2(t_0)}.$$

Then, from the results (7) and (8), the spin-down power from eq. (1), the surface magnetic field minimal strength from eq. (3) and the characteristic age from eq. (2) have been estimated:

$$\begin{aligned} -\frac{dE_{rot}}{dt} &= (33813 \pm 1) \times 10^{32} \text{ erg/s} \\ B_{min} &= (318728 \pm 6) \times 10^7 \text{ G} \\ \tau &= (17197.7 \pm 0.6) \text{ yr} \end{aligned}$$

where the uncertainties were obtained by propagating those of  $f$  and  $\dot{f}$ . Moreover a neutron star moment of inertia of  $10^{45} \text{ g cm}^2$  has been considered [6].

**Light curves** Putting the test results (7) and (8) in the timing model (5), light curves have been obtained. The latter are shown in Fig. (3) for  $0.1 - 1 \text{ GeV}$ ,  $> 1 \text{ GeV}$  and  $> 0.1 \text{ GeV}$ . Since the curve was not easily visible, because one peak was around the null phase, the offset 0.15 has been fixed in the phase formula (6).

For each light curve a fit with the least squares method has been performed, using the sum of a constant and two gauss distributions as model function:

$$c + d_1 e^{-\frac{(x-\mu_1)^2}{2\sigma_1^2}} + d_2 e^{-\frac{(x-\mu_2)^2}{2\sigma_2^2}},$$

where  $\mu_i$  and  $\sigma_i$  are, respectively, mean and standard deviation of the gauss distributions, while  $c$ ,  $d_i$  are constants.

Then the Pearson's  $\chi^2$  test has been used. The counts for each bin have a poisson distribution, then the standard deviation for each bin is given by the root of its counts value. But, because of the central limit theorem, the poisson distribution asymptotically tends to be a gauss distribution for higher counts value. The histogram probability density function is a multinomial distribution of the single bin's distributions. Let  $k$  be the number of bins,  $N$  the total number of counts and  $p_i$  the counts probability for each bin. Thereby the logarithm of the likelihood function  $L$  is approximable as

$$\log(L) \approx -\frac{1}{2} \sum_{i=1}^N \frac{(k_i - Np_i)^2}{Np_i}$$

which is generally accepted as close enough to  $-\frac{1}{2}\chi^2_{k-1}$  when all the expected numbers of events per bin  $Np_i$  are greater than 5. See [7].

The best fits and the goodness of fit test results are showed in Tab. 1.

As expected from the photon energy distribution in Fig. 1, the photons' counts decrease with increasing energy. Instead the signal to noise ratio increases. Indeed to this latter fact is that the area surrounding the source is largely populated by low-energy photons by the Galactic diffuse emission, as observed in Fig. 2. Moreover there is a clear evolution of the light-curve shape with increasing energy: let's call peaks P1 and P2 in phase ascending order, then there is a slightly shift of both peaks, but mainly of P1. Indeed they come closer to each other. Furthermore, as the energy increases, the height of P1 increases as well, but peak P2 always dominates slightly over P1.

## 6 $P-\dot{P}$ diagram

J2021+3651 has been put in a  $P-\dot{P}$  diagram (Fig. 4) along with some radio pulsars from the ATNF catalog [8].

## 7 Conclusions

From the analysis of the gamma rays detected from September 21th, 2008 at 00:00 UTC to December 20th 2008 at 00:00 UTC, it has turned out that J2021+3651 is a pulsar with the characteristic age  $(17197.7 \pm 0.6)$  yr and the magnetic field with minimum intensity  $(318728 \pm 6) \times 10^7$  G. It rotates at the frequency  $(9639344919 \pm 1) \times 10^{-9} \text{ s}^{-1}$  decreasing by the rate  $(88855 \pm 3) \times 10^{-16} \text{ s}^{-2}$ . The latter is due to a decreasing energy rate of  $(33813 \pm 1) \times 10^{32} \text{ erg/s}$ . Furthermore, the evolution from low to high energies was highlighted. Indeed the ratio between the height of P1 and P2 increases from  $0.88214 \pm 0.00003$  to  $0.9364 \pm 0.0001$ . Finally the SNR increases with energy and there is a phase change of the peaks which lead peak's phase difference from  $0.531 \pm 0.005$  to  $0.469 \pm 0.007$ .

## References

- [1] [LAT Data Analysis Tools](#).
- [2] [LAT Data Selection Recommendations](#).
- [3] [Caveats About Analyzing LAT](#).
- [4] [Arrival Time Correction](#).
- [5] Buccheri, R., et al. 1983, "Search for pulsed  $\gamma$ -ray emission from radio pulsars in the COS-B data", [A&A](#) 128, 245-251.
- [6] A. A. Abdo et al 2009, "Pulsed gamma-rays from PSR J2021+3651 with the FERMI Large Area Telescope", [ApJ](#) 700 1059.
- [7] James, Frederick E. Statistical Methods in Experimental Physics. 2.nd ed. New Jersey, 2006.
- [8] [ATNF Pulsar Catalogue](#).

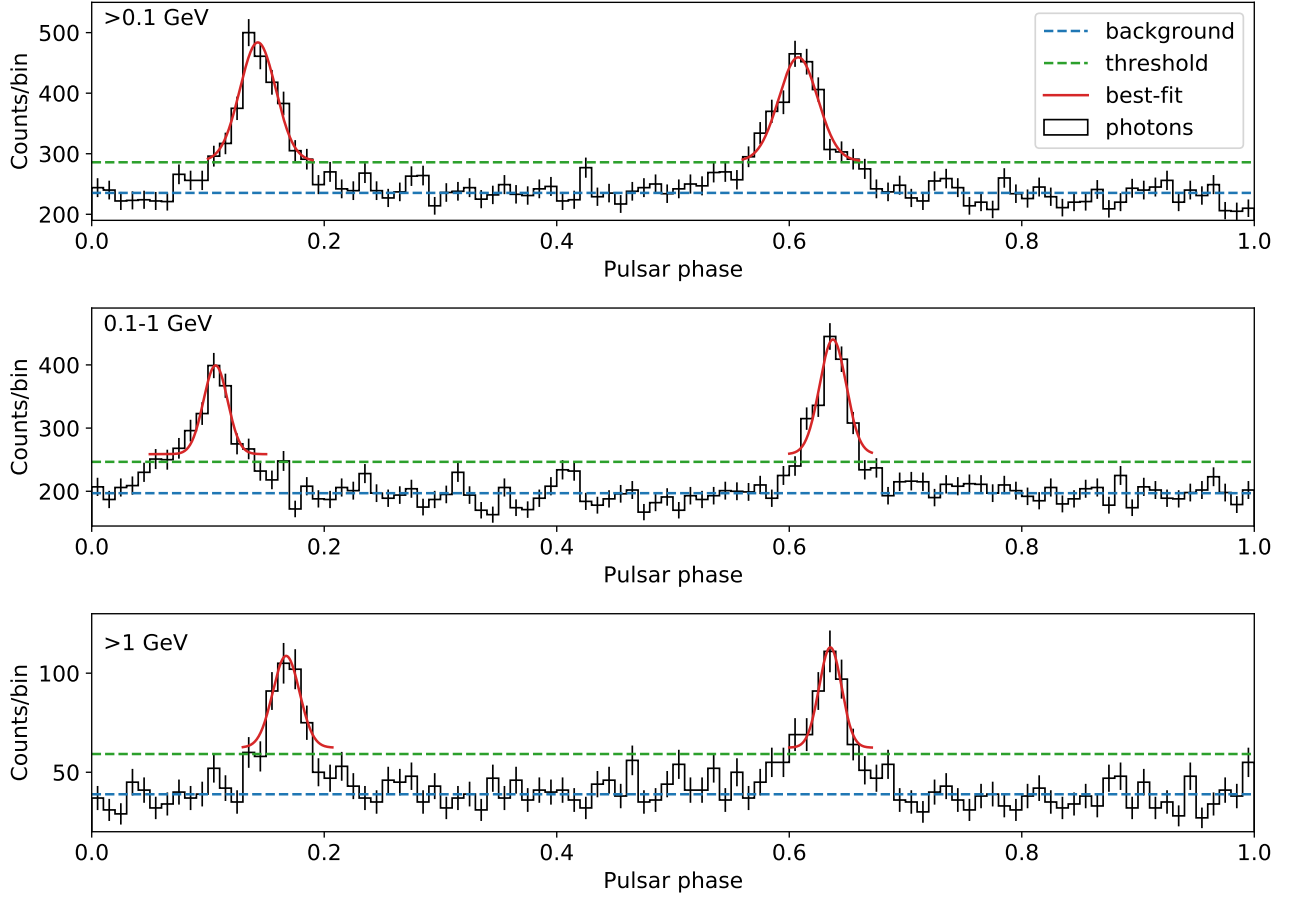


Figure 3: Gamma-ray histogram shown over one period of rotation with a resolution of 100 phase bins (corresponding to 0.01 ms per bin). The first takes into account all the photons with energy above 0.1 GeV, meanwhile the middle one takes into account the lower ones (0.1-1 GeV) and the last with higher ones (above 1 GeV). The red and green dotted lines indicate the background and threshold level respectively. The latter is defined as three times the background standard deviation above the background mean. The background was taken from 0.3 to 0.5 and from 0.8 to 1.0.

symbol	>0.1 GeV	0.1-1 GeV	>1 GeV
$\chi^2$	14	9	2
$\nu$	11	7	3
$p$	0.2	0.2	0.7
P1	$0.14 \pm 0.01$	$0.11 \pm 0.01$	$0.15 \pm 0.01$
P2	$0.61 \pm 0.01$	$0.64 \pm 0.01$	$0.63 \pm 0.01$
P2-P1	$0.46 \pm 0.01$	$0.531 \pm 0.005$	$0.469 \pm 0.007$
P1/P2	$1.05361 \pm 0.00003$	$0.88214 \pm 0.00003$	$0.9364 \pm 0.0001$
$c$	$(28 \pm 1) \times 10$	$259 \pm 8$	$62 \pm 4$
$f_1$	$(17 \pm 2) \times 10$	$(14 \pm 2) \times 10$	$46 \pm 6$
$\mu_1$	$0.607 \pm 0.001$	$0.107 \pm 0.001$	$0.167 \pm 0.001$
$\sigma_1$	$0.017 \pm 0.002$	$0.011 \pm 0.002$	$0.012 \pm 0.002$
$f_2$	$(19 \pm 2) \times 10$	$(182 \pm 2) \times 10$	$51 \pm 6$
$\mu_2$	$0.142 \pm 0.001$	$0.638 \pm 0.001$	$0.637 \pm 0.001$
$\sigma_2$	$0.015 \pm 0.002$	$0.011 \pm 0.001$	$0.009 \pm 0.001$

Table 1: For each energy band the table shows Pearson's  $\chi^2$ , number of degrees of freedom  $\nu$ , p-value  $p$ , model's parameters ( $c$ ,  $f_{1/2}$ ,  $\mu_{1/2}$ ,  $\sigma_{1/2}$ ), phase of the top point of peaks P1 (left peak in Fig. 3) and P2 (right) indicated by the peak's name, their difference P2-P1 and the ratio of their heights P1/P2. The uncertainties of fits results come from the fits itself, while the uncertainty of P1 and P2 is the bin's width of the histograms. Then P2-P1 and P1/P2 uncertainties come from the propagations of the latter.

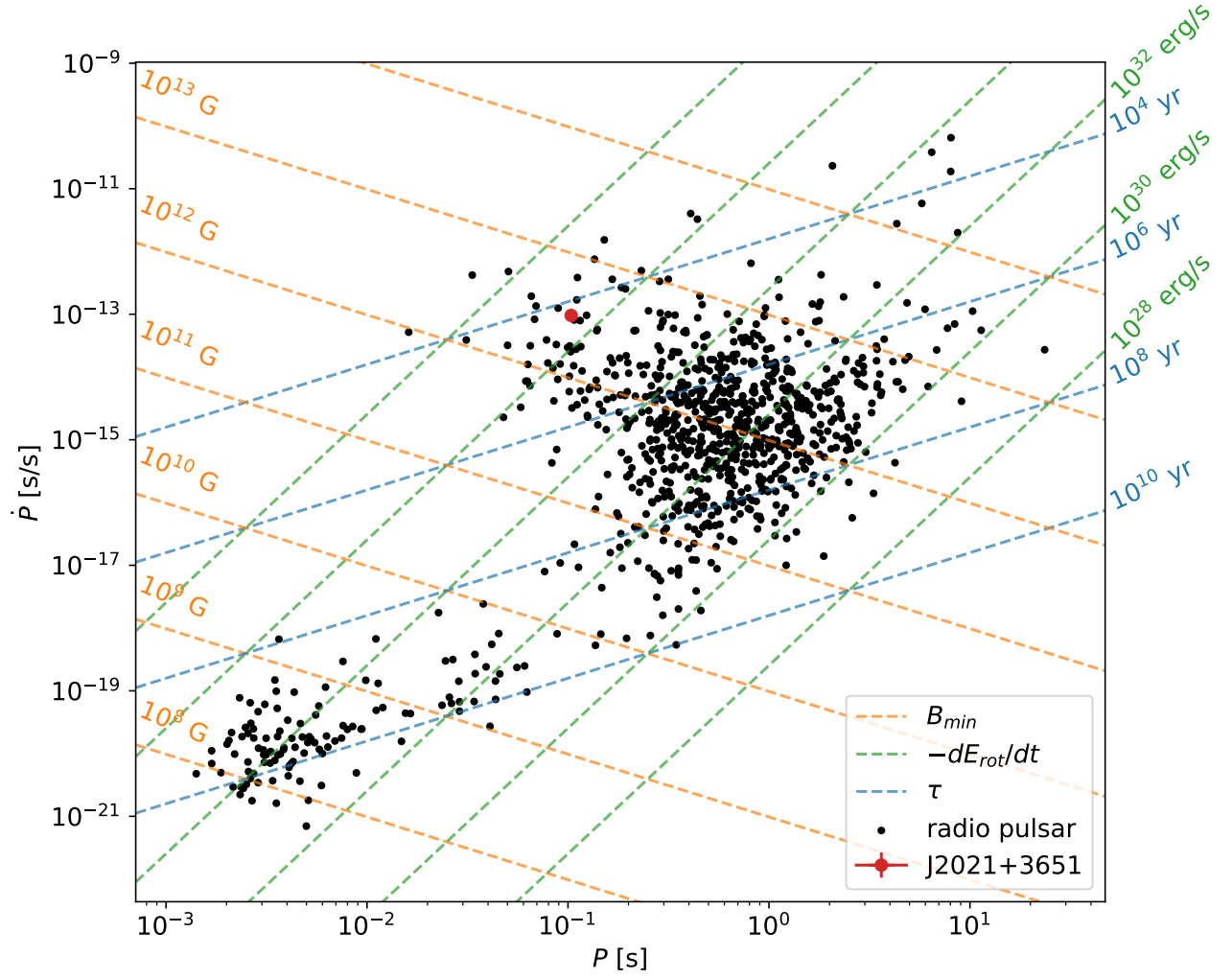


Figure 4:  $P - \dot{P}$  diagram, where  $P$  is the rotation period of pulsars and  $\dot{P}$  is the rate of the period change. It makes evident the characteristics quantities of pulsars, such as the minimum magnetic field strength in orange, the characteristic age in blue and the rotational brightness in green. The black dots are some radio pulsars from the ATNF catalog, while the red dot is the pulsar J2021+3651.